

Ocean wave spectrum and dissipation rate derived from CMOD4 model function

David R. Lyzenga

General Dynamics Advanced Information Systems, Ann Arbor, Michigan, USA

Received 5 December 2003; revised 5 May 2004; accepted 21 May 2004; published 27 July 2004.

[1] A simplified version of the energy balance equation is solved to obtain an expression for the ocean wave equilibrium spectrum, which is then used with a two-scale electromagnetic scattering model to calculate the radar cross section of the ocean surface. Two parameters in the energy balance equation are adjusted to minimize the difference between the calculated radar cross-section values and those given by the CMOD4 model function over a range of incidence angles and look directions, and for a series of wind speeds. The RMS difference between the CMOD4 and two-scale radar cross-section values using this model is 0.16 dB for incidence angles from 25° to 45° and wind speeds from 5 to 15 m/s. The slope variances computed from this model also agree fairly well with those measured by Cox and Munk. However, since the largest wave number influencing the C-band backscatter is approximately 200 rad/m, the spectrum is probably not valid beyond this wave number. Finally, since the spectrum is determined by the relative magnitudes of the wave growth and dissipation rates, some inferences about these parameters can be drawn. Assuming the exponential growth rate parameter to be equal to previous measurements, the dissipation rate implied by this model is more than an order of magnitude larger than that due to molecular viscosity for wind speeds greater than 7 m/s. This conclusion is consistent with observations by Jähne and Riemer, which also indicated a dissipation rate much larger than the viscous dissipation rate at high wind speeds.

INDEX TERMS: 4275 Oceanography: General: Remote sensing and electromagnetic processes (0689); 4504 Oceanography: Physical: Air/sea interactions (0312); 4560 Oceanography: Physical: Surface waves and tides (1255); *KEYWORDS:* ocean wave spectrum, radar backscatter, remote sensing

Citation: Lyzenga, D. R. (2004), Ocean wave spectrum and dissipation rate derived from CMOD4 model function, *J. Geophys. Res.*, 109, C07019, doi:10.1029/2003JC002237.

1. Introduction

[2] The state of the ocean surface is dependent on the wind speed and direction, as well as a number of other parameters such as the fetch and duration of the wind, the air-sea temperature difference, the water depth, the current gradients, and the presence of surfactant materials. If the wind speed is constant for a sufficiently long time and fetch is sufficiently large, the sea surface is believed to approach an equilibrium state. The surface elevation or wave height frequency spectrum under these conditions was proposed by Pierson and Moskowitz [1964] to have the form

$$S_{pm}(\omega) = \alpha_{pm} g^2 \omega^{-5} \exp\{-0.74(\omega_o/\omega)^4\} \quad (1)$$

where $\alpha_{pm} = 0.0081$ and $\omega_o = g/U_{19.5}$, g is the gravitational acceleration, and $U_{19.5}$ is the wind speed measured at a height of 19.5 m above the surface. The technology for measuring wave propagation directions was relatively undeveloped at the time of this publication, so no

directional distribution was specified. Mitsuyasu *et al.* [1975] subsequently made directional measurements using a cloverleaf buoy, which they described with an angular distribution of the form

$$\Phi(\phi) = A_s \cos^{2s}(\phi/2), \quad (2)$$

where $A_s = \frac{1}{2\pi} \frac{\Gamma^2(s+1)}{\Gamma(2s+1)} 2^{2s}$ so that $\int_0^{2\pi} \Phi(\phi) d\phi = 1$. The resulting values of s were found to be a maximum at the spectral peak and to fall off rapidly with frequency above the spectral peak. Hasselmann *et al.* [1973, 1980] extended the Pierson-Moskowitz spectrum to include fetch effects, and also derived the expressions

$$\begin{aligned} s &= 6.97(\omega/\omega_p)^{4.06} & \omega < \omega_p \\ s &= 9.77(\omega/\omega_p)^{-\mu} & \omega > \omega_p, \end{aligned} \quad (3)$$

for the s parameter in equation (2), where ω_p is the peak frequency, $\mu = 2.33 + 1.45(U/c_p - 1.17)$, and c_p is the phase velocity at the spectral peak. Further refinements regarding both the angular distribution and the spectral shape were made by Donelan *et al.* [1985], and more detailed models

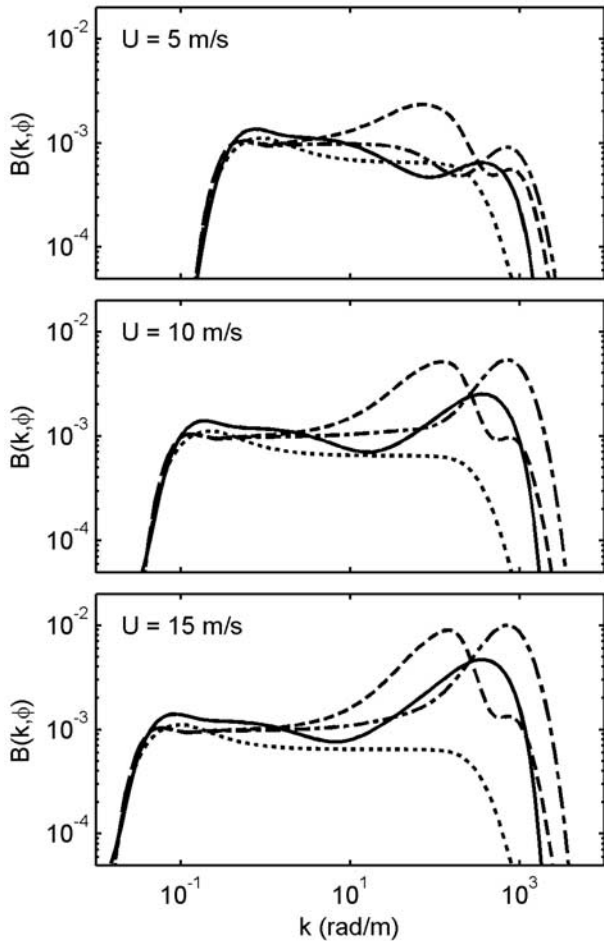


Figure 1. Comparison of spectral models of *Pierson and Moskowitz* [1964] (dotted line), *Apel* [1994] (dash-dotted line), *Romeiser et al.* [1997] (dashed line), and *Elfouhaily et al.* [1997] (solid line) in wind direction, for wind speeds of 5, 10, and 15 m/s. The first three spectra have been symmetrized with respect to the wind direction for comparison with the *Elfouhaily et al.* spectrum, which is inherently symmetrical.

for short wavelengths were constructed by *Durden and Vesecky* [1985], *Plant* [1986], and *Donelan and Pierson* [1987] using radar backscatter and surface slope statistics as well as in situ measurements. These models were also based partially on energy balance considerations similar to those discussed in the following section.

[3] Recently, the development of optical surface measurement techniques [e.g., *Jähne and Riemer*, 1990; *Hara et al.*, 1994] and an expanded inventory of radar backscatter measurements have stimulated several attempts to develop a spectral form covering the entire range of wavelengths. *Apel* [1994] proposed a form consisting of the product of three terms, one describing the low-frequency behavior, the second describing the high-frequency behavior, and the third describing the angular distribution. *Caudal and Hauser* [1996] corrected certain problems with the angular distribution in *Apel's* spectrum, and proposed an alternate form based on a variety of radar backscatter measurements. *Romeiser et al.* [1997] further modified both the wave

number and angular dependence of the short-wave portion of *Apel's* spectrum in order to better predict radar backscatter measurements. Finally, *Elfouhaily et al.* [1997] derived a unified spectrum using only optical measurements for the short-wave portion along with previous formulations for the long-wave portion of the spectrum. These spectra are plotted in Figure 1. This figure shows the dimensionless curvature spectrum, which is obtained by multiplying the wave height spectrum by k^4 where k is the wave number. Also shown in this figure is the *Pierson-Moskowitz* spectrum, converted into wave number space using the gravity-capillary dispersion relation. It is interesting that the use of the full dispersion relation produces a high wave number cutoff in the *Pierson-Moskowitz* spectrum, and that this spectrum forms an approximate lower bound to the more recently developed spectra.

2. Spectral Energy Balance Model

[4] Large-scale wave prediction models such as *WAM* [*Komen et al.*, 1994] are based on solutions of the spectral energy or action balance equation. The action balance equation has also been used to describe the interaction of short waves with variable surface currents [e.g., *Lyzenga and Bennett*, 1988]. These models include various formulations of the net source function for wave energy or action. A simplified form of the net source function can be written in terms of the dimensionless curvature spectrum $B(\mathbf{k}) = k^4 S(\mathbf{k})$ as

$$F_s(\mathbf{k}) = \alpha(\mathbf{k}, \mathbf{U}) + [\beta(\mathbf{k}, \mathbf{U}) - 4\nu k^2]B(\mathbf{k}) - \gamma(\mathbf{k})B(\mathbf{k})^2, \quad (4)$$

where $\alpha(\mathbf{k}, \mathbf{U})$ is the linear growth rate and $\beta(\mathbf{k}, \mathbf{U})$ is the exponential growth rate for the wind vector \mathbf{U} and wave number vector \mathbf{k} , $\nu = 0.01 \text{ cm}^2/\text{s}$ is the molecular kinematic viscosity of seawater, and the last term represents the dissipation due to wave breaking. Nonlinear energy transfer among wave numbers is neglected in this formulation. The equilibrium spectrum is defined as the solution of the equation $F_s(\mathbf{k}) = 0$; for the source function in equation (4), this equilibrium spectrum can be written as

$$B_o(\mathbf{k}) = \frac{1}{2\gamma} \left(\beta' + \sqrt{\beta'^2 + 4\alpha\gamma} \right) = B_2(\mathbf{k}) + \sqrt{B_2^2(\mathbf{k}) + B_1^2(\mathbf{k})}, \quad (5)$$

where $\beta' = \beta(\mathbf{k}, \mathbf{U}) - 4\nu k^2$. Note that $B_o(\mathbf{k})$ is always positive even though β' can become negative at high wave numbers.

[5] We assume that the linear growth term dominates at low wave numbers, and in this region the equilibrium spectrum is equal to the *Pierson-Moskowitz* spectrum (converted to wave number coordinates using the gravity wave dispersion relation) with the angular distribution given by equations (2) and (3). Thus the first component of the spectrum has the form

$$B_1(\mathbf{k}) = \sqrt{\alpha/\gamma} = \frac{1}{2} \alpha_{\text{pm}} \exp\{-0.74 (k_o/k)^2\} \Phi(\phi'), \quad (6)$$

where $\phi' = \phi - \phi_w$ is the angle between the wind and the wave propagation direction. Next, we assume that we can

express the exponential growth rate as $\beta = (b_0 + b_1 \cos \phi' + b_2 \cos 2\phi')k/c$ and the dissipation term as $\gamma = \gamma_o \omega$. This form for the growth rate has approximately the same wave number dependence as that suggested by *Plant* [1982], and allows for a fairly general angular distribution. For simplicity, we have neglected capillarity and wind speed effects on the phase velocity in this expression, however, so the wave number dependence of β is not exactly the same as that of *Plant* [1982]. The wind speed dependence is not specified here since the fitting procedure described below is repeated for each wind speed, and so the wind speed dependence arises from that procedure. The second component of the spectrum then has the form

$$B_2(\mathbf{k}) = \frac{\beta'}{2\gamma} = \frac{1}{2\gamma_o} (b_0 + b_1 \cos \phi' + b_2 \cos 2\phi' - 4\nu kc)/c^2. \quad (7)$$

The constants b_0 , b_1 , b_2 , and γ_o were chosen to optimize the agreement between the radar cross sections computed from this spectrum and the CMOD4 model function, as described in the following sections.

3. Radar Backscatter Model

[6] The radar backscatter from the ocean surface is calculated using the two-scale model [*Wright*, 1968; *Chan and Fung*, 1977], which involves an integral over the large-scale surface slopes η_x and η_y , i.e.,

$$\bar{\sigma}^o(\theta, \phi) = \int_{-\infty}^{\infty} \int_{-\infty}^{\infty} \sigma^o(\eta_x, \eta_y) p(\eta_x, \eta_y) d\eta_x d\eta_y, \quad (8)$$

where $\sigma^o(\eta_x, \eta_y)$ is the radar cross section per unit area for a surface element with slopes η_x and η_y , and $p(\eta_x, \eta_y)$ is the large-scale slope probability density function multiplied by the factor

$$a(\eta_x, \eta_y) = 1 - (\eta_x \cos \phi + \eta_y \sin \phi) \tan \theta$$

$$(\eta_x \cos \phi + \eta_y \sin \phi) < \cot \theta \quad (9)$$

$$a(\eta_x, \eta_y) = 0 \quad (\eta_x \cos \phi + \eta_y \sin \phi) > \cot \theta,$$

where θ is the incidence angle and ϕ is the look direction relative to the x - z plane. This factor accounts for the projected area of each facet in the line of sight direction (Appendix A). However, since there is some disagreement about this term, we have also repeated the calculations discussed in section 5 without this term, i.e., with $a(\eta_x, \eta_y) = 1$. The radar cross section for a given facet is a function of the surface slopes η_x and η_y , for two reasons: first, because of the change in the local incidence and azimuth angles, and second, because of the rotation of the polarization basis vectors in the local coordinate system, relative to those in the global coordinate system.

[7] In order to facilitate computation of these effects, it is convenient to describe the orientation of each facet by means of the surface normal vector,

$$\mathbf{n} = \frac{(-\eta_x, -\eta_y, 1)}{\sqrt{1 + \eta_x^2 + \eta_y^2}} = (\sin \theta_n \cos \phi_n, \sin \theta_n \sin \phi_n, \cos \theta_n), \quad (10)$$

where θ_n is the angle between the surface normal and the z axis, and ϕ_n is the angle of rotation about this axis. The slope integration in the two-scale model can then be written as an integral over these angles, i.e.,

$$\bar{\sigma}^o(\theta, \phi) = \int_0^{\pi/2} \int_{-\pi}^{\pi} \sigma^o(\theta_n, \phi_n) p_n(\theta_n, \phi_n) d\theta_n d\phi_n, \quad (11)$$

where $p_n(\theta_n, \phi_n) = p(\eta_x, \eta_y) n_z^{-3} \sin \theta_n$ (see Appendix B). The angles describing the surface normal can also be defined relative to the observation direction instead of the z axis. The redefined angle θ'_n is then equivalent to the local incidence angle, and ϕ'_n is equivalent to the angle of rotation of the plane of polarization relative to each facet. The radar cross section for each facet is calculated using the small perturbation method (SPM) for local incidence angles greater than about 8.6° and the geometric optics method for zero local incidence angle, resulting in the expression

$$\sigma^o(\theta'_n, \phi'_n) = 16\pi k^4 S_o(k_b, \phi') |G_p(\theta'_n, \phi'_n)|^2 + \frac{R(0)\delta(\theta'_n)}{2n_z \sin \theta'_n}, \quad (12)$$

where k is the electromagnetic wave number, $S_o(k_b, \phi') = \frac{1}{2}[B(k_b, \phi') + B(k_b, \phi' + \pi)] H(k_b - k_c) k_b^{-4}$ is the symmetrized small-scale wave height spectral density at the Bragg wave number $k_b = 2k \sin \theta'_n$ and the local azimuth angle ϕ' , $H(k)$ is the Heaviside step function, $k_c = 0.3k$ is the scale separation or cutoff wave number, and $R(0)$ is the Fresnel reflectivity for normal incidence. The coefficients $G_p(\theta'_n, \phi'_n)$ for HH and VV polarization are given by

$$G_h(\theta'_n, \phi'_n) = g_h(\theta'_n) \cos^2 \phi'_n + g_v(\theta'_n) \sin^2 \phi'_n \quad (13)$$

$$G_v(\theta'_n, \phi'_n) = g_v(\theta'_n) \cos^2 \phi'_n + g_h(\theta'_n) \sin^2 \phi'_n,$$

where $g_h(\theta'_n)$ and $g_v(\theta'_n)$ are the SPM scattering coefficients for HH and VV polarization, respectively, i.e.,

$$g_h(\theta) = R_h \cos^2 \theta$$

$$g_v(\theta) = R_v \cos^2 \theta + \frac{1}{2} (1 + R_v)^2 \left(1 - \frac{1}{\epsilon}\right) \sin^2 \theta, \quad (14)$$

where $R_h = \frac{k_z - k'_z}{k_z + k'_z}$, $R_v = \frac{\epsilon k_z - k'_z}{\epsilon k_z + k'_z}$, $k_z = k \cos \theta$, $k'_z = k \sqrt{\epsilon - \sin^2 \theta}$, and ϵ is the complex permittivity or dielectric constant of the surface.

[8] Using a Gaussian or normal slope probability density function, this model predicts the same radar cross section in the upwind and downwind directions. The upwind-downwind asymmetry observed in measurements over the ocean can be reproduced by either using a non-Gaussian (skewed) slope distribution or by introducing hydrodynamic modulation effects. Using the latter approach, we multiply the integrand in equation (8) or equation (11) by the factor $1 + m' \eta_u$ where η_u is the component of the surface slope in the upwind direction and m' is related to the imaginary part

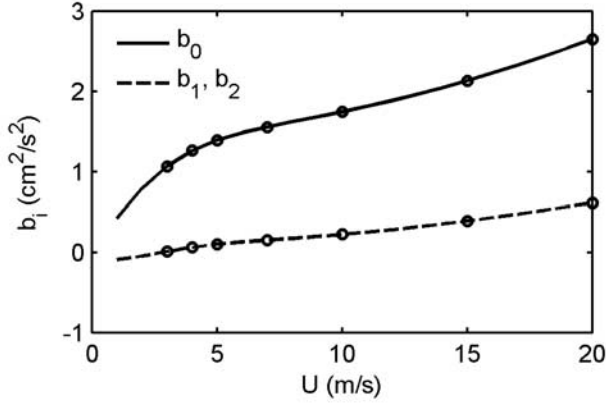


Figure 2. Inferred growth rate parameters, assuming a nominal viscous dissipation rate, versus wind speed.

of the modulation transfer function (mtf), as discussed in Appendix C. The slope probability density function (without the projected-area factor) is given by

$$p(\eta_x, \eta_y) = \frac{1}{2\pi\sigma_c\sigma_u} \exp\left\{-\frac{1}{2}\left(\frac{\eta_c^2}{\sigma_c^2} + \frac{\eta_u^2}{\sigma_u^2}\right)\right\}, \quad (15)$$

where $\eta_c = \eta_x \sin \phi_w + \eta_y \cos \phi_w$ and $\eta_u = \eta_x \cos \phi_w - \eta_y \sin \phi_w$ are the crosswind and upwind slopes,

$$\sigma_c^2 = \int_0^{k_c} \int_{-\pi}^{\pi} k^{-1} \sin^2 \phi' B(k, \phi') dk d\phi' \quad (16)$$

$$\sigma_u^2 = \int_0^{k_c} \int_{-\pi}^{\pi} k^{-1} \cos^2 \phi' B(k, \phi') dk d\phi'$$

are the corresponding slope variances, and $k_c = 0.3k$ is the same cutoff wave number as used for the SPM calculation.

4. CMOD4 Model Function

[9] The CMOD4 model function was derived and validated using a large number of C-band, V-polarization radar backscatter measurements made by the ERS-1 scatterometer over an incidence angle range from 18° to 57° and a wind speed range from about 0–20 m/s [Stoffelen and Anderson, 1997]. The form of this model function is

$$\sigma^\circ(\text{dB}) = a_0 + 16 \log_{10}(1 + a_1 \cos \phi + a_2 \cos 2\phi) + \varepsilon_r(\theta), \quad (17)$$

where

$$a_0 = c_1 + c_2x + c_3(3x^2 - 1)/2 + \gamma f_1(U),$$

$$\gamma = c_4 + c_5x + c_6(3x^2 - 1)/2,$$

$$f_1(U) = -10 \quad U + U_o \leq 10^{-10},$$

$$f_1(U) = \log_{10}(U + U_o) \quad 10^{-10} < U + U_o \leq 5, \quad (18)$$

$$f_1(U) = \sqrt{(U + U_o)/3.2} \quad U + U_o > 5,$$

$$U_o = c_7 + c_8x + c_9(3x^2 - 1)/2,$$

$$x = (\theta - 40^\circ)/25^\circ,$$

$$a_1 = c_{10} + c_{11}U + (c_{12} + c_{13}U)f_2(U), \quad (19)$$

$$f_2(U) = \tanh[(2.5(x + 0.35))] - 0.61(x + 0.35),$$

$$a_2 = 0.42[1 + c_{16}(c_{17} + x)(c_{18} + U)] \tanh[c_{14} + c_{15}(1 + x)U], \quad (20)$$

and $\varepsilon_r(\theta)$ is a tabulated residual factor between -0.35 and $+0.31$ dB (which was neglected in this work). The constants c_1 through c_{18} are given by Stoffelen and Anderson [1997]. Note, however, that the constants c_1 through c_6 are one tenth of those of Stoffelen and Anderson, because the radar cross section is given in decibels here.

5. Fitting Procedure and Results

[10] The spectrum given in equations (5)–(7) was used in the two-scale model described in section 3, and the parameters b_0 , b_1 , b_2 , and γ_o in equation (7) were adjusted so as to minimize the difference (in dB) between the resulting radar cross-section values and those given by the CMOD4 model function over the incidence angle range from 25° to 45° and over all look directions. The minimization was done using the algorithm of Nelder and Mead [1965] in two stages: first, the CMOD4 radar cross sections were symmetrized with respect to the look direction by taking the average of $\sigma^\circ(\theta, \phi)$ and $\sigma^\circ(\theta, \phi + \pi)$ for each ϕ , and these values were fit using the two-scale model with zero mtf. This resulted in the spectral model described below. Then, the procedure was repeated with the actual (asymmetric) CMOD4 values using this spectrum and varying the mtf in order to optimize the fit at each incidence angle. Applying this procedure over a range of wind speeds, it was observed that the quality of the fit is not significantly reduced if a constant value of $\gamma_o = 0.33$ is used and if the values of b_1 and b_2 are assumed to be equal. The optimum values of the two remaining parameters (b_0 and b_1) are plotted versus wind speed in Figure 2. These values were then fit to the equations

$$b_0 = \frac{a_{01}U + a_{03}U^3 + a_{04}U^4}{a_{02} + U^2} \times 10^{-4} \text{m}^2/\text{s}^2 \quad (21)$$

$$b_1 = \frac{a_{11}(U - U_1) + a_{13}(U - U_1)^3 + a_{14}(U - U_1)^4}{a_{12} + (U - U_1)^2} \times 10^{-4} \text{m}^2/\text{s}^2, \quad (22)$$

where $a_{01} = 12.766$, $a_{02} = 29.180$, $a_{03} = 0.0851$, $a_{04} = 0.0013$, $a_{11} = 0.6562$, $a_{12} = 11.217$, $a_{13} = 0.0185$, $a_{14} = 0.0010$, and $U_1 = 2.8686$ m/s. The solid lines in Figure 2 represent these fits.

[11] The wave spectra computed using these equations for wind speeds of 5, 10, and 15 m/s are shown in Figures 3 and 4. The mtf values required to best reproduce the upwind-downwind asymmetry in the CMOD4 radar cross-section values are plotted versus incidence angle at the same wind speeds in Figure 5. These values are within the range of those estimated by Hara and Plant [1994] from radar measurements during the SAXON-FPN experiment. Finally, radar cross-section values from the present model are

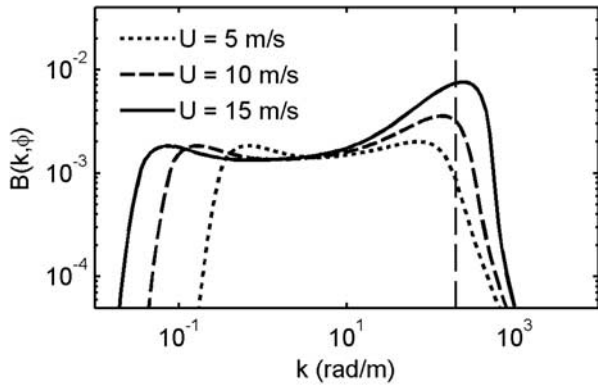


Figure 3. Inferred spectrum at $\phi = 0$ for three wind speeds. Vertical dashed line indicates the maximum wave number influencing the radar backscatter over the range of incidence angles considered in this study, as discussed in section 6.

compared with CMOD4 values in Figure 6. The root-mean-square (RMS) difference between the values plotted in Figure 6 is 0.16 dB. For comparison, the RMS difference for the same set of points using the spectrum of *Elfouhaily et al.* [1997] is slightly over 3 dB, which is perhaps not surprising since no radar data were used in the derivation of this spectrum. One problem in using the *Elfouhaily* spectrum is that it is symmetric with respect to the wind direction, so that it does not contain any information about the relative amplitudes of upwind versus downwind propagating waves. Although the spectrum used in the radar backscatter model itself must be symmetrized as discussed in section 3, the one-sided or nonsymmetric spectrum is needed to calculate the hydrodynamic modulation effects discussed in Appendix C. Thus it is not possible to account for upwind/downwind differences in the radar cross section due to these effects using *Elfouhaily's* spectrum as originally formulated, although it is possible to modify this spectrum to make it nonsymmetric, for example by replacing their angular dependence with a form such as that given by equation (2) with the parameter s selected to produce the same upwind-crosswind ratio as in the original spectrum.

[12] If the projected-area factor in equation (9) is not included in the two-scale model, both the derived wave

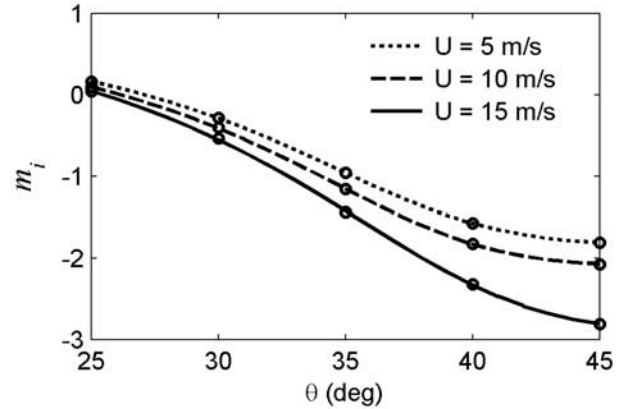


Figure 5. Imaginary part of hydrodynamic modulation transfer function required for best fit to CMOD4 data.

spectrum and the agreement with CMOD4 radar cross-section values are virtually unchanged, but the mtf values required to produce the best fit are roughly 30% larger than those shown in Figure 5. This difference is probably not large enough to draw any conclusions about the correctness of the projected area factor. This issue could perhaps be resolved by direct comparisons between two-scale model predictions and exact numerical calculations of the backscatter, particularly at larger incidence angles where this factor is expected to have a larger effect.

[13] The same model can also be used to calculate the radar cross section for horizontal polarization, which is of interest for the interpretation of RADARSAT synthetic aperture radar data, for example. The C-band horizontal polarization radar cross sections predicted from our model are shown in Figure 7. These results are compared with values computed from the equation

$$\sigma_H^o = \left(\frac{1 + \alpha \tan^2 \theta}{1 + 2 \tan^2 \theta} \right)^2 \sigma_V^o \quad (23)$$

proposed by *Thompson et al.* [1998], using $\alpha = 0.6$ as originally proposed by these authors and also using $\alpha = 1$ as suggested by *Vachon and Dobson* [2000] and *Horstmann et al.* [2000]. The results from the present model are close to

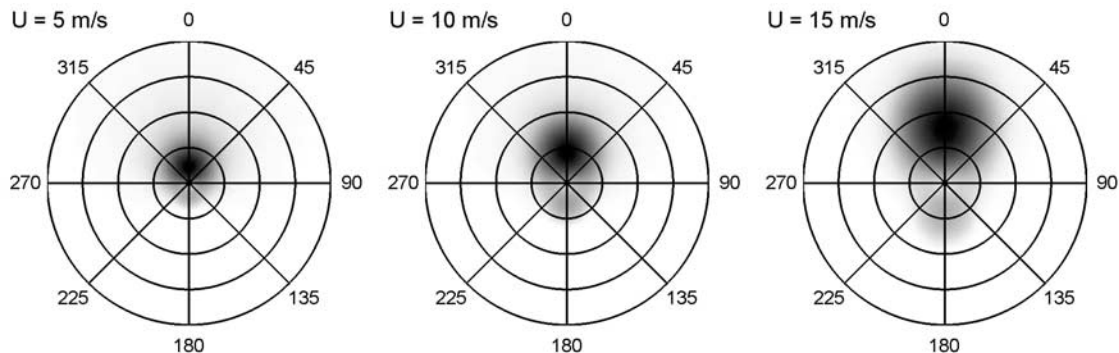


Figure 4. Gray-scale plots of two-dimensional curvature spectra at three wind speeds. Maximum wave number (outer circle) is 200π rad/m.

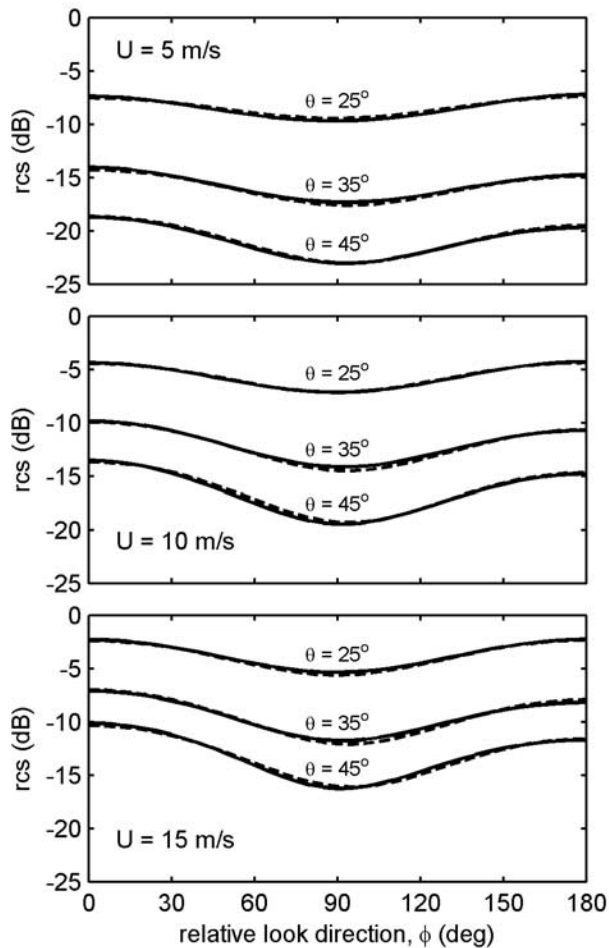


Figure 6. Comparison of VV-polarization model predictions (solid curves) with CMOD4 radar cross sections (dashed curves) for three incidence angles and wind speeds.

the $\alpha = 1$ values at 25° incidence, but are closer to the $\alpha = 0.6$ values at larger incidence angles. Note that our model also predicts a larger upwind/downwind asymmetry for HH-polarization than for VV-polarization, and therefore a larger asymmetry than is given by equation (23). Further testing of these models could be done using data from the recently launched Envisat advanced synthetic aperture radar, which is capable of operating at both HH and VV polarizations.

6. Discussion

[14] The equilibrium spectrum derived here is broadly similar to the earlier models shown in Figure 1, although it appears to cut off at a somewhat lower wave number. However, the largest wave number that actually influences the microwave backscatter for the frequency (5.3 GHz) and incidence angle range (25° – 45°) considered here is approximately 200 rad/m, including surface tilt effects, so the details of the spectrum beyond this wave number may not be reliable. Comparisons with higher frequency (e.g., K-band) measurements or model functions could be used to refine the spectrum at higher wave numbers. Inclusion of additional mechanisms such as the generation of parasitic capillary

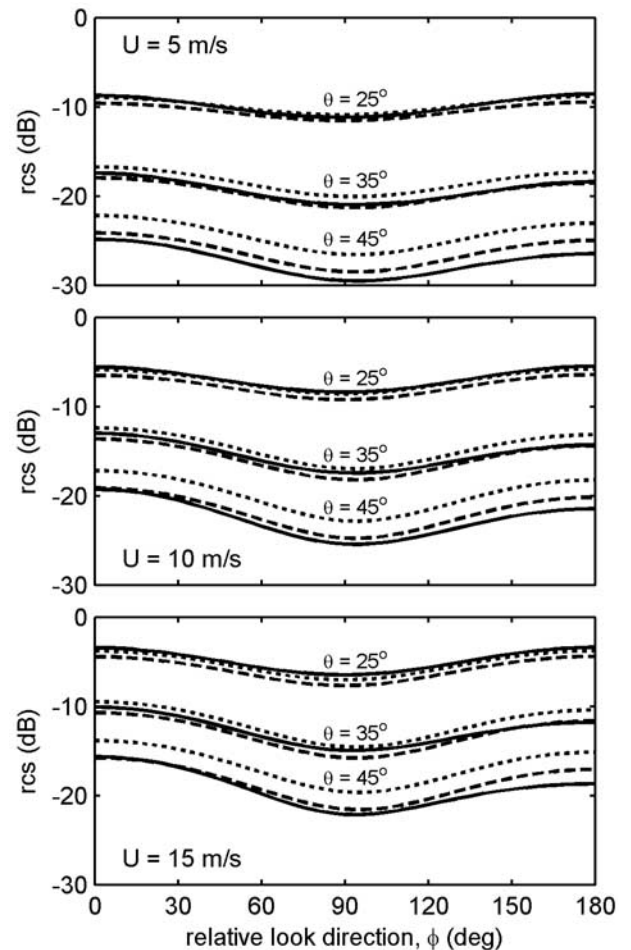


Figure 7. HH-polarization radar cross sections predicted by the present model (solid curves) compared with predictions from equation (23) using $\alpha = 0.6$ (dashed curves) and $\alpha = 1$ (dotted curves).

waves may be required to construct a physical model for these wave numbers.

[15] Another test of the spectral model is provided by integral properties such as the height or slope variance. The

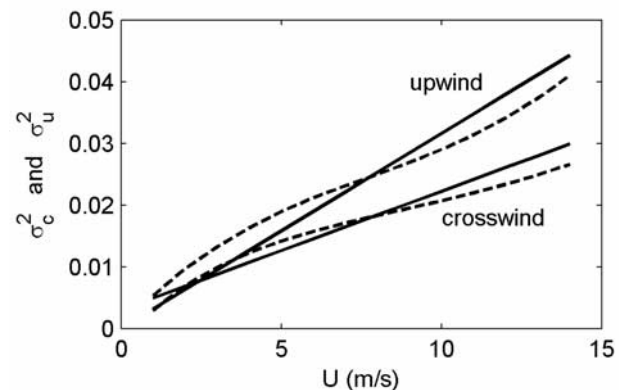


Figure 8. Comparison of upwind and crosswind slope variances from the spectrum described in this paper (dashed curves) with measurements by *Cox and Munk* [1954] (solid curves).

height variance is determined by the low wave number portion of the spectrum and is therefore essentially the same as that of the Pierson-Moskowitz spectrum. The upwind and crosswind slope variances, which are more sensitive to the behavior at high wave numbers, are compared with those measured by *Cox and Munk* [1954] in Figure 8, over the range of wind speeds (1 to 14 m/s) occurring during Cox and Munk's measurements. The agreement is fairly close, considering the fact that these measurements were not used during the development of the model, and thus represent a truly independent data set. On the other hand, the significance of this comparison is unclear in view of the uncertainty in the spectrum for wave numbers larger than 200 rad/m, as discussed above, since these wave numbers have a strong effect on the slope variances.

[16] Finally, since the model described here involves the growth rate parameter β , it is of interest to compare this growth rate with previous formulations and measurements. Comparisons with the growth rates of *Snyder et al.* [1981], *Plant* [1982], and *Donelan and Pierson* [1987] are shown in Figure 9. These growth rates were calculated using the full gravity-capillary dispersion relation including the wind speed dependence of the phase velocity as given by *Plant and Wright* [1980]. The growth rate resulting from our fitting procedure is much smaller than these previously published values. However, since the spectrum is determined by the ratio of the wave growth rate to the dissipation rate, this discrepancy can be taken as an indication that the dissipation rates in equation (7) are too small. The scale factor required to bring our growth rate into agreement with that of *Plant* [1982] is shown in Figure 10 as a function of the wind speed. We interpret this as the factor by which the dissipation rate exceeds that due to molecular viscosity. This result is consistent with the conclusion of *Jähne and Riemer* [1990] that the dissipation rate at high wind speeds and high wave numbers is at least an order of magnitude larger than the viscous dissipation rate.

Appendix A: Projected-Area Factor

[17] The slope probability density function $p(\eta_x, \eta_y)$ multiplied by $d\eta_x d\eta_y$ may be interpreted as the probability that a vertically directed ray passing through the surface will

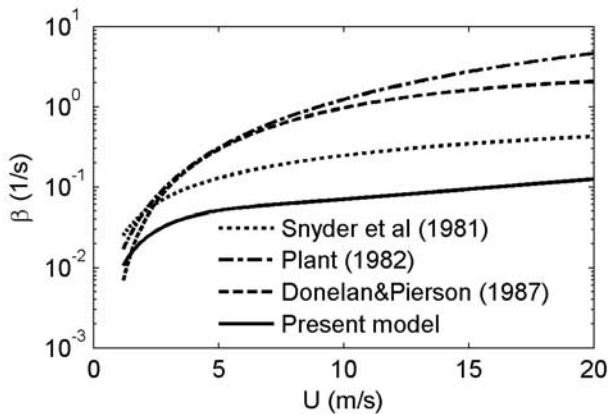


Figure 9. Comparison of the exponential growth rate parameter β at $k = 100$ rad/m with the formulations of *Snyder et al.* [1981], *Plant* [1982], and *Donelan and Pierson* [1987].

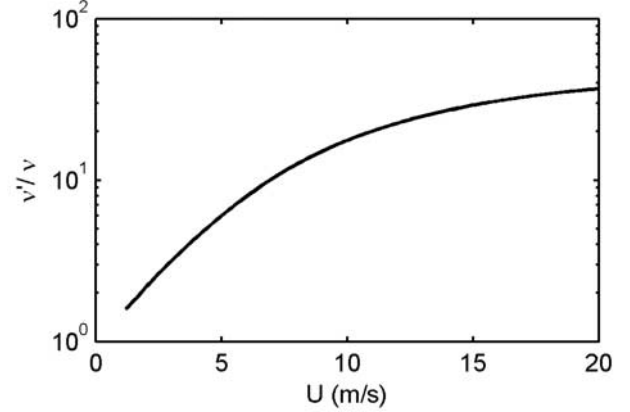


Figure 10. Scale factor on the dissipation rate required to bring growth rate into agreement with that of *Plant* [1982].

encounter a slope in the range from η_x to $\eta_x + d\eta_x$ in the x -direction and from η_y to $\eta_y + d\eta_y$ in the y -direction. This probability is equivalent to the vertical projection of the total area of the surface elements having slopes in this range, per unit horizontal area. A surface element of area dA having this slope will have a vertically projected area (i.e., the area projected onto a horizontal surface) of $n_z dA$ where $n_z = \mathbf{n} \cdot \mathbf{z}$ is the z -component of the unit surface normal vector. Therefore the total surface area of the surface elements having slopes in this range is $dA = n_z^{-1} p(\eta_x, \eta_y) d\eta_x d\eta_y$. The projected area of these surface elements in the direction \mathbf{k} is

$$dA' = \mathbf{n} \cdot \mathbf{k} dA = (\mathbf{n} \cdot \mathbf{k} / \mathbf{n} \cdot \mathbf{z}) p(\eta_x, \eta_y) d\eta_x d\eta_y \quad \mathbf{n} \cdot \mathbf{k} > 0. \quad (\text{A1})$$

[18] However, when viewed from this direction, the unit horizontal area has a projected area of $k_z = \mathbf{k} \cdot \mathbf{z}$. The probability that a ray in this direction will intercept one of these surface elements is equal to the projected area of the surface elements divided by the projected area of the unit horizontal surface, i.e.,

$$dA' / k_z = (\mathbf{n} \cdot \mathbf{k} / n_z k_z) p(\eta_x, \eta_y) d\eta_x d\eta_y \quad \mathbf{n} \cdot \mathbf{k} > 0. \quad (\text{A2})$$

[19] Thus the apparent slope probability density function for the look direction \mathbf{k} is $p'(S_x, S_y) = (\mathbf{n} \cdot \mathbf{k} / n_z k_z) p(S_x, S_y)$. Using $\mathbf{k} = (\sin \theta \cos \phi, \sin \theta \sin \phi, \cos \theta)$ the projected-area factor can be written as

$$a(\eta_x, \eta_y) = \mathbf{n} \cdot \mathbf{k} / n_z k_z = 1 - (\eta_x \cos \phi + \eta_y \sin \phi) \tan \theta. \quad (\text{A3})$$

[20] This is the same factor as used by *Chan and Fung* [1977], although the derivation of this factor is not presented there.

Appendix B: Integration Over Surface Normal Angles

[21] Expressing the surface normal in terms of the angles θ_n and ϕ_n as defined in equation (10), we can write the slope components as

$$\eta_x = -\tan \theta_n \cos \phi_n \quad (\text{B1})$$

$$\eta_y = -\tan \theta_n \sin \phi_n.$$

The change of the variables of integration from (η_x, η_y) to (θ_n, ϕ_n) then involves the Jacobian

$$\frac{\partial(\eta_x, \eta_y)}{\partial(\theta_n, \phi_n)} = \begin{vmatrix} \partial\eta_x/\partial\theta_n & \partial\eta_y/\partial\theta_n \\ \partial\eta_x/\partial\phi_n & \partial\eta_y/\partial\phi_n \end{vmatrix} = \tan\theta_n \sec^2\theta_n = \frac{\sin\theta_n}{n_z^3}, \quad (\text{B2})$$

which allows the slope integration to be written as equation (11). However, the surface normal can also be expressed in terms of the orthogonal unit vectors \mathbf{k} , \mathbf{h} , and \mathbf{v} as

$$\mathbf{n} = \mathbf{v} \sin\theta'_n \cos\phi'_n + \mathbf{h} \sin\theta'_n \sin\phi'_n + \mathbf{k} \cos\theta'_n, \quad (\text{B3})$$

where \mathbf{k} is in the direction of observation (pointing toward the radar antenna), \mathbf{h} is the horizontal polarization basis vector ($\mathbf{h} \cdot \mathbf{z} = 0$ and $\mathbf{h} \cdot \mathbf{k} = 0$), and \mathbf{v} is the vertical polarization basis vector ($\mathbf{v} \cdot \mathbf{h} = 0$ and $\mathbf{v} \cdot \mathbf{k} = 0$). Using $\mathbf{h} = \mathbf{z} \times \mathbf{k} / \sin\theta$ and $\mathbf{v} = \mathbf{h} \cdot \mathbf{k} = (\mathbf{k} \cos\theta - \mathbf{z}) / \sin\theta$, we have $\mathbf{h} \cdot \mathbf{x} = -\sin\phi$, $\mathbf{h} \cdot \mathbf{y} = \cos\phi$, $\mathbf{v} \cdot \mathbf{x} = \cos\theta \cos\phi$, $\mathbf{v} \cdot \mathbf{y} = \cos\theta \sin\phi$, and $\mathbf{v} \cdot \mathbf{z} = -\sin\theta$.

[22] The components of the normal vector in the xyz coordinate system are then given by

$$\begin{aligned} n_x &= \mathbf{n} \cdot \mathbf{x} = \cos\theta \cos\phi \sin\theta'_n \cos\phi'_n - \sin\phi \sin\theta'_n \sin\phi'_n \\ &\quad + \sin\theta \cos\phi \cos\theta'_n, \\ n_y &= \mathbf{n} \cdot \mathbf{y} = \cos\theta \sin\phi \sin\theta'_n \cos\phi'_n + \cos\phi \sin\theta'_n \sin\phi'_n \\ &\quad + \sin\theta \sin\phi \cos\theta'_n, \\ n_z &= \mathbf{n} \cdot \mathbf{z} = -\sin\theta \sin\theta'_n \cos\phi'_n + \cos\theta \cos\theta'_n, \end{aligned} \quad (\text{B4})$$

and the components of the surface slope are

$$\begin{aligned} \eta_x &= -\frac{n_x}{n_z} \\ &= \frac{(\sin\theta \cos\theta'_n + \cos\theta \sin\theta'_n \cos\phi'_n) \cos\phi - (\sin\theta'_n \sin\phi'_n) \sin\phi}{\sin\theta \sin\theta'_n \cos\phi'_n - \cos\theta \cos\theta'_n} \end{aligned} \quad (\text{B5})$$

$$\begin{aligned} \eta_y &= -\frac{n_y}{n_z} \\ &= \frac{(\sin\theta \cos\theta'_n + \cos\theta \sin\theta'_n \cos\phi'_n) \sin\phi + (\sin\theta'_n \sin\phi'_n) \cos\phi}{\sin\theta \sin\theta'_n \cos\phi'_n - \cos\theta \cos\theta'_n}. \end{aligned} \quad (\text{B6})$$

[23] The Jacobian relating the variables θ'_n and ϕ'_n to the surface slope is given by

$$\frac{\partial(\eta_x, \eta_y)}{\partial(\theta'_n, \phi'_n)} = \frac{\sin\theta'_n}{n_z^3}, \quad (\text{B7})$$

so the integral over θ'_n and ϕ'_n can be written in the same form as equation (11). The advantage of using these variables is that θ'_n is equal to the local incidence angle, and ϕ'_n is equal to the angle of rotation of the polarization basis vectors in the local coordinate system.

[24] To calculate the rotation of the plane of polarization, note that in the local coordinate system (i.e., in a coordinate

system aligned with the local surface normal) the polarization basis vectors are given by $\mathbf{h}' = \mathbf{n} \times \mathbf{k} / \sin\theta'_n$ and $\mathbf{v}' = (\mathbf{k} \cos\theta'_n - \mathbf{n}) / \sin\theta'_n$. The angle (α) between these basis vectors and those in the global coordinate system is therefore

$$\begin{aligned} \sin\alpha &= \mathbf{h}' \cdot \mathbf{v} = \frac{(\mathbf{n} \times \mathbf{k}) \cdot (\mathbf{k} \cos\theta'_n - \mathbf{z})}{\sin\theta'_n \sin\theta'_n} = \frac{(\mathbf{k} \cdot \mathbf{n}) \cdot \mathbf{z}}{\sin\theta'_n \sin\theta'_n} \\ &= \frac{(\mathbf{z} \cdot \mathbf{k}) \cdot \mathbf{n}}{\sin\theta'_n \sin\theta'_n}. \end{aligned} \quad (\text{B8})$$

Using $\mathbf{z} \cdot \mathbf{k} = \mathbf{h} \sin\theta$ and $\mathbf{h} \cdot \mathbf{n} = \sin\theta'_n \sin\phi'_n$, we then have $\sin\alpha = \sin\phi'_n$, or $\alpha = \phi'_n$.

[25] The only remaining issue is the calculation of the local azimuth angle or look direction, which we define as the angle between the projections onto the local surface of the look direction \mathbf{k} and the wind vector \mathbf{U} . The projection of \mathbf{k} onto the local surface is $\mathbf{k}'_h = \mathbf{k} - \mathbf{n} \cos\theta'_n$, and the projection of \mathbf{U} is $\mathbf{U}' = \mathbf{U} - (\mathbf{U} \cdot \mathbf{n})\mathbf{n} = \mathbf{U} - (n_x \cos\phi_w + n_y \sin\phi_w)\mathbf{n}$ where ϕ_w is the wind direction relative to the x axis. The angle between these projections is then given by

$$\begin{aligned} \cos\phi' &= \frac{\mathbf{k}'_h \cdot \mathbf{U}'}{|\mathbf{k}'_h| |\mathbf{U}'|} \\ &= \frac{(k_x - n_x \cos\theta'_n) \cos\phi_w + (k_y - n_y \cos\theta'_n) \sin\phi_w}{\sin\theta'_n \sqrt{1 - (n_x \cos\phi_w + n_y \sin\phi_w)^2}}, \end{aligned} \quad (\text{B9})$$

$$\begin{aligned} \sin\phi' &= \frac{(\mathbf{U}' \times \mathbf{k}'_h) \cdot \mathbf{n}}{|\mathbf{k}'_h| |\mathbf{U}'|} = \frac{(\mathbf{U} \times \mathbf{k}) \cdot \mathbf{n}}{|\mathbf{k}'_h| |\mathbf{U}'|} \\ &= \frac{(k_y n_z - k_z n_y) \cos\phi_w + (k_x n_z - k_z n_x) \sin\phi_w}{\sin\theta'_n \sqrt{1 - (n_x \cos\phi_w + n_y \sin\phi_w)^2}}, \end{aligned} \quad (\text{B10})$$

$$\tan\phi' = \frac{(k_y n_z - k_z n_y) \cos\phi_w + (k_x n_z - k_z n_x) \sin\phi_w}{(k_x - n_x \cos\theta'_n) \cos\phi_w + (k_y - n_y \cos\theta'_n) \sin\phi_w}. \quad (\text{B11})$$

Appendix C: Hydrodynamic Modulation Effects

[26] Hydrodynamic interactions between long and short waves can cause spatial variations in the small-scale roughness. These interactions can be described by means of the dimensionless modulation transfer function $m = m_r + im_i$, which is defined such that the fractional change in the short wave spectral density is given by

$$f'(x, y) = \text{Re} \iint mk \psi(k_x, k_y) e^{i(k_x x + k_y y)} dk_x dk_y, \quad (\text{C1})$$

where $\psi(k_x, k_y)$ is the one-sided Fourier transform of the surface elevation (i.e., the integral of the three-dimensional Fourier transform over positive frequencies). Using this definition, the surface elevation is given by

$$\eta(x, y) = \text{Re} \iint \psi(k_x, k_y) e^{i(k_x x + k_y y)} dk_x dk_y,$$

and the surface slopes in the upwind and crosswind directions are given by

$$\begin{aligned}\eta_u(x, y) &= \text{Re} \iint ik_u \psi(k_x, k_y) e^{i(k_x x + k_y y)} dk_x dk_y \\ \eta_c(x, y) &= \text{Re} \iint ik_c \psi(k_x, k_y) e^{i(k_x x + k_y y)} dk_x dk_y,\end{aligned}\quad (\text{C2})$$

where $k_u = k_x \cos \phi_w + k_y \sin \phi_w$ and $k_c = k_y \cos \phi_w - k_x \sin \phi_w$. The one-sided Fourier transform also has the properties

$$\begin{aligned}\langle \psi(k_x, k_y) \psi(k'_x, k'_y) \rangle &= 0 \\ \langle \psi(k_x, k_y) \psi^*(k'_x, k'_y) \rangle &= 2S(k_x, k_y) \delta(k_x - k'_x) \delta(k_y - k'_y),\end{aligned}$$

where $S(k_x, k_y)$ is the one-sided wave height spectrum. The covariance between the short wave spectrum and the upwind surface slope is then given by

$$\langle f \eta_u \rangle = \iint m_i k k_u S(k_x, k_y) dk_x dk_y. \quad (\text{C3})$$

The predicted or expected value of the fractional spectral modulation is therefore proportional to the upwind surface slope, i.e., $f = m' \eta_u$, where

$$m' = \frac{\langle f \eta_u \rangle}{\langle \eta_u^2 \rangle} = \frac{\iint m_i k k_u S(k_x, k_y) dk_x dk_y}{\iint k_u^2 S(k_x, k_y) dk_x dk_y}. \quad (\text{C4})$$

This effect is incorporated into the two-scale model by multiplying the radar cross section of each facet within the slope integral by the factor $1 + m' \eta_u$.

[27] **Acknowledgments.** This work was sponsored by the Office of Naval Research, award N00014-00-D-0114 (delivery order 0006). The author would like to thank William Plant and an anonymous reviewer for their helpful comments on this paper.

References

- Apel, J. R. (1994), An improved model of the ocean surface wave vector spectrum and its effect on radar backscatter, *J. Geophys. Res.*, *99*, 16,269–16,291.
- Caudal, G., and D. Hauser (1996), Directional spreading function of the sea spectrum at short scale, inferred from multifrequency radar observations, *J. Geophys. Res.*, *101*, 16,601–16,613.
- Chan, H. L., and A. K. Fung (1977), A theory of sea scatter at large incidence angles, *J. Geophys. Res.*, *82*, 3439–3444.
- Cox, C., and W. Munk (1954), Measurement of the roughness of the sea surface from photographs of the sun's glitter, *J. Opt. Soc. Am.*, *44*, 838–850.
- Donelan, M. A., and W. J. Pierson (1987), Radar scattering and equilibrium ranges in wind-generated waves with application to scatterometry, *J. Geophys. Res.*, *92*, 4971–5029.
- Donelan, M. A., J. Hamilton, and W. H. Hui (1985), Directional spectra of wind generated waves, *Philos. Trans. R. Soc. London, Ser. A*, *315*, 509–562.
- Durden, S. P., and J. F. Vesecky (1985), A physical radar cross-section model for a wind-driven sea with swell, *IEEE J. Oceanic Eng.*, *OE-10*, 445–451.
- Elfouhaily, T., B. Chapron, K. Katsaros, and D. Vandemark (1997), A unified directional spectrum for long and short wind-driven waves, *J. Geophys. Res.*, *102*, 15,781–15,796.
- Hara, T., and W. J. Plant (1994), Hydrodynamic modulation of short wind-wave spectra by long waves and its measurement using microwave backscatter, *J. Geophys. Res.*, *99*, 9767–9784.
- Hara, T., E. J. Bock, and D. R. Lyzenga (1994), In situ measurements of capillary-gravity wave spectra using a scanning laser slope gauge and microwave radars, *J. Geophys. Res.*, *99*, 12,593–12,602.
- Hasselmann, D. E., M. Dunkel, and J. A. Ewing (1980), Directional wave spectra observed during JONSWAP 1973, *J. Phys. Oceanogr.*, *10*, 1264–1280.
- Hasselmann, K., et al. (1973), Measurements of wind-wave growth and swell decay during the Joint North Sea Wave Project (JONSWAP), *Dtsch. Hydrogr. Z.*, *A8(12)*, 1–95.
- Horstmann, J., W. Kock, S. Lehner, and R. Tonboe (2000), Wind retrieval over the ocean using synthetic aperture radar with C-band HH polarization, *IEEE Trans. Geosci. Remote Sens.*, *38*, 2122–2131.
- Jähne, B., and K. S. Riemer (1990), Two-dimensional wavenumber spectra of small-scale water surface waves, *J. Geophys. Res.*, *95*, 11,531–11,546.
- Komen, G. J., L. Cavaleri, M. Donelan, K. Hasselmann, S. Hasselmann, and P. A. E. M. Janssen (1994), *Dynamics and Modelling of Ocean Waves*, 560 pp., Cambridge Univ. Press, New York.
- Lyzenga, D. R., and J. R. Bennett (1988), Full-spectrum modeling of SAR internal wave signatures, *J. Geophys. Res.*, *93*, 12,345–12,354.
- Mitsuyasu, H., F. Tasai, T. Suhara, S. Mizuno, M. Ohkuso, T. Honda, and K. Rikiishi (1975), Observations of the directional spectrum of ocean waves using a cloverleaf buoy, *J. Phys. Oceanogr.*, *5*, 750–760.
- Nelder, J. A., and R. Mead (1965), A simplex method for function minimization, *Comput. J.*, *7*, 308–313.
- Pierson, W. J., and L. Moskowitz (1964), A proposed spectral form for fully developed seas based on the similarity theory of S. A. Kitaigorodskii, *J. Geophys. Res.*, *69*, 5181–5190.
- Plant, W. J. (1982), A relationship between wind stress and wave slope, *J. Geophys. Res.*, *87*, 1961–1967.
- Plant, W. J. (1986), A two-scale model of short wind-generated waves and scatterometry, *J. Geophys. Res.*, *91*, 10,735–10,749.
- Plant, W. J., and J. W. Wright (1980), Phase speeds of upwind and downwind traveling short gravity waves, *J. Geophys. Res.*, *85*, 3304–3310.
- Romeiser, R., W. Alpers, and V. Wisman (1997), An improved composite surface model for the radar backscattering cross section of the ocean surface: 1. Theory of the model and optimization/validation by scatterometer data, *J. Geophys. Res.*, *102*, 25,237–25,250.
- Snyder, R. L., F. W. Dobson, J. A. Elliot, and R. B. Long (1981), Array measurements of atmospheric pressure fluctuations above gravity waves, *J. Fluid Mech.*, *102*, 1–59.
- Stoffelen, A., and D. Anderson (1997), Scatterometer data interpretation: Estimation and validation of the transfer function CMOD4, *J. Geophys. Res.*, *102*, 5767–5780.
- Thompson, D. R., T. M. Elfouhaily, and B. Chapron (1998), Polarization ratio for microwave backscattering from the ocean surface at low to moderate incidence angles, paper presented at International Geoscience and Remote Sensing Symposium, IEEE Geosci. and Remote Sens. Soc., Seattle, Wash.
- Vachon, P. W., and F. W. Dobson (2000), Wind retrieval from RADARSAT SAR images: Selection of a suitable C-band HH polarization wind retrieval model, *Can. J. Remote Sens.*, *26*, 306–313.
- Wright, J. W. (1968), A new model for sea clutter, *IEEE Trans. Antennas Propag.*, *AP-16*, 217–223.

D. R. Lyzenga, General Dynamics Advanced Information Systems, Ann Arbor, MI 48113-4008, USA. (david.lyzenga@gd-ais.com)